Effect of annealing on the microstructure, ordering and microhardness of ball milled cubic (L1$_2$) titanium trialuminide intermetallic powder

R.A. Varin [a,*], J. Bystrzycki [a,1], A. Calka [b]

[a] *Department of Mechanical Engineering, University of Waterloo, Waterloo, Ontario, Canada N2L 3G1*
[b] *Department of Materials Engineering, University of Wollongong, Wollongong, New South Wales 2522, Australia*

Abstract

Ball milled powders of cubic (L1$_2$) titanium trialuminide modified with Mn, possessing nanocrystalline structure, were annealed at 600°C and 1000–1100°C. The best results for the calculation of the nanocrystalline grain size upon annealing from the X-ray diffraction (XRD) patterns, were obtained using the Cauchy/Gaussian approximation for both the instrumental broadening and nanocrystallite size/lattice strain separation. The nanocrystallite size increased upon annealing from 1 to 240 min at 600°C, from the initial several nanometers for the as-milled powders, to 30–140 nm for the annealed powders. This nanocrystalline grain growth is accompanied by a continuous increase of the long-range order (LRO) parameter, from zero to ~0.8–0.9 after annealing at 600°C for 240 min. However, a phenomenal thermal stability of nanocrystalline grains is manifested in the fact that only very few powder particles exhibited the formation of micrometer-sized grains after annealing at the 1000–1100°C range. The observed differential thermal analysis (DTA) exothermic peaks around 410–430°C (peak I) and 570°C (peak II) are interpreted as the atomic re-ordering and the phase restoration peak, respectively. The observed hardening of the "outer layer" and "no core" particles upon annealing at 600°C is discussed in terms of nanograin boundaries age-hardening mechanism due to the pick-up of interstitials (carbon and/or nitrogen) and their preferential segregation at the nanograin boundaries. The reversal of the process, i.e. desegregation, might be responsible for the observed softening of the "outer layer" and "no core" particles upon annealing at the 1000–1100°C range, without any apparent microstructural changes observable under optical/scanning microscope. © 1999 Elsevier Science Ltd. All rights reserved.

Keywords: A. Nanostructured intermetallics; A. Trialuminides; B. Order/disorder transformations; B. Thermal stability; D. Microstructure

1. Introduction

In our previous publication [1] we discussed the evolution of morphology, microstructure and microhardness brought about by the use of mechanical milling applied to the as-cast and homogenized Mn-modified, single-phase, cubic (L1$_2$) titanium trialuminide (L1$_2$ Al$_3$Ti(Mn)). Mechanical (ball) milling was conducted under shearing mode in a controlled ball movement mill [2], where after a long-time milling (over 200 h a number of the larger powder particles comprised a work-hardened "core" surrounded by a heavily deformed "outer layer" containing nanometer crystallites (or grains).

Other smaller particles did not contain any "cores" (called "no core" particles). X-ray diffraction (XRD) and transmission electron microscopy studies (TEM) have shown that nanocrystallites are formed in the heavily deformed powder particles as a result of controlled ball milling under shearing mode. It has also been shown that such a microstructural evolution during ball milling of cubic titanium trialuminides is accompanied by a progressive disordering of their crystalline lattice.

An important technological step following the production of powders is their compaction into a bulk material with a density as close to the theoretical density as possible. In particular, for nanocrystalline powders it would be desirable to retain the nanocrystalline structure, at least partially if not fully, after compaction. However, achieving such a goal is not a trivial task. As a first step, a thorough knowledge of the microstructural

---

* Corresponding author.
[1] NATO Science Fellow on leave of absence from the Department of Materials Technology, Military University of Technology, Kaliskiego 2, 01–489 Warsaw, Poland.

line for the disordered (dis) and homogenized reference (hr) powder, respectively.

Fig. 2 shows the LRO parameter for the powder milled for 208 h and annealed at 600°C for various times. The measured degree of order increases quickly with increasing annealing time, attaining a nearly complete ordered state (LRO&0.9) after 30 to 60 min. It can be seen in this figure that the LRO parameter calculated from the (110/220) pair is systematically greater than that from the (100/200) pair. Similar structural anisotropy of (110/220) versus (100/200) was reported by Morris and Günter [5] and suggests a tetragonal arrangement for the third atomic species (Mn), even though the crystal retains the ordered L1$_2$ structure.
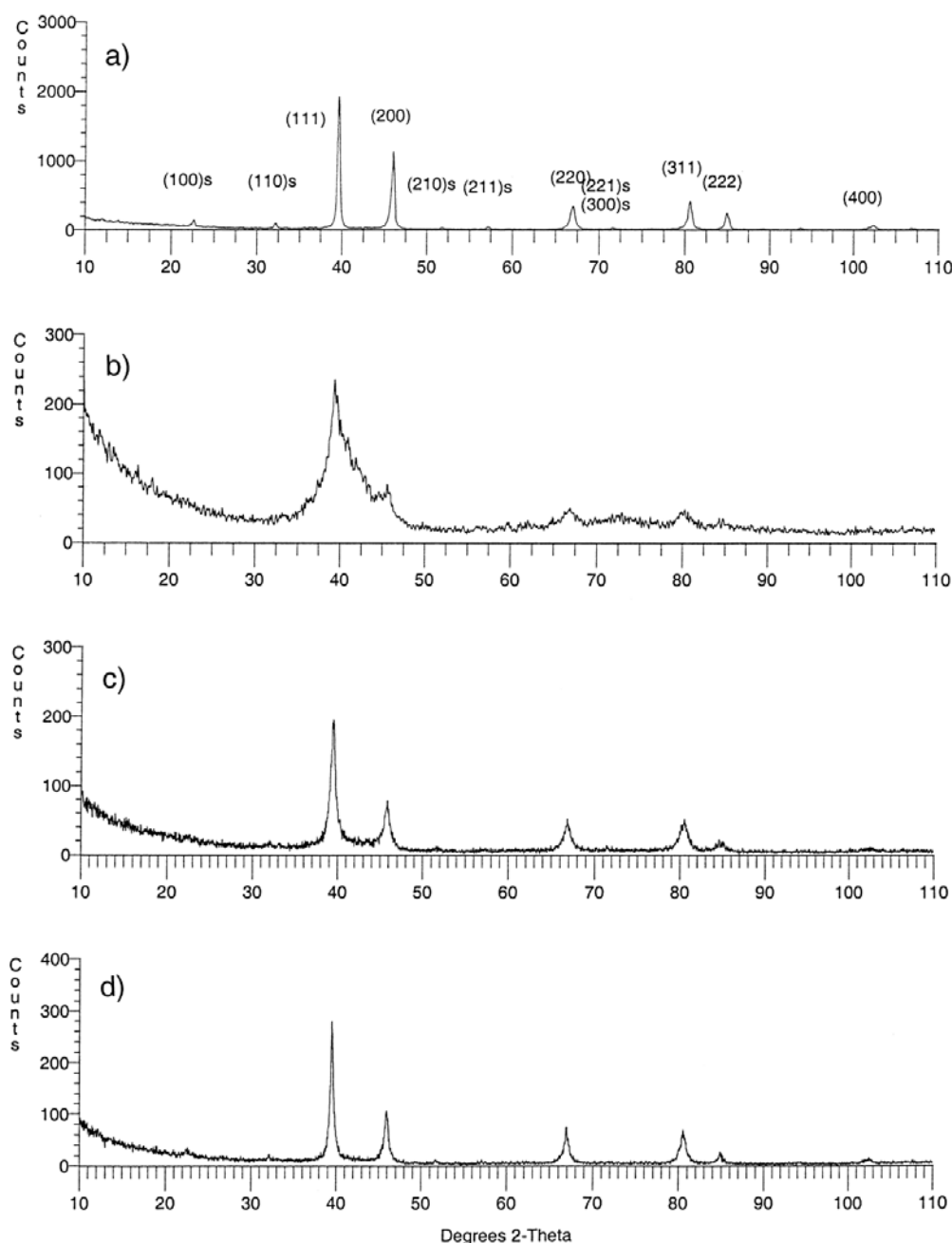

Fig. 1. X-ray diffraction (XRD) patterns of cubic (L1$_2$) titanium trialuminide powders: (a) standard annealed (800°C/3 h) pulverized ingot; (b) powder milled for 208 h; (c) the same milled powder subsequently annealed at 600°C for 1 min; (d) annealed for 60 min.
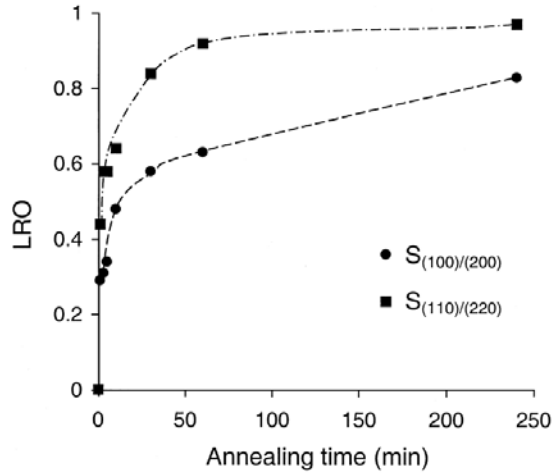
Fig. 2. Degree of long-range order parameter LRO, as a function of annealing time at 600°C for the trialuminide powder milled for 208 h.

3.2. Methodology of crystallite and domain size calculations

Each X-ray diffraction line profile obtained in a diffractometer is broadened due to instrumental and physical (crystallite size and lattice strains) factors [6]. Therefore, the first indispensable step preparatory to the calculation of crystallite size and lattice strain from the recorded XRD scan is a determination of the "pure" diffraction line profile for a given reflection whose breadth depends solely on the physical factors [6]. This "pure" line profile is extracted by removing (deconvoluting) the instrumental broadening factor from the experimental line profile. Only then the "pure" line profile can be used for calculating the crystallite size and lattice strain.

Simple equations or graphs based on line profiles of assumed analytical forms can be used for the instrumental broadening correction [6]. In the present work, the instrumental broadening-corrected "pure" line profile breadth of each reflection was calculated from the parabolic approximation correction [6]:

$$\delta(2\theta) = B\left(1 - \frac{b^2}{B^2}\right) \ (\text{rad}) \tag{2}$$

where B and b are the breadths (in radians) of the same Bragg peak from the XRD scans of the experimental and reference powder, respectively. The reference powder was the same powdered titanium trialuminide ingot annealed at 800°C for 3 h. Both B and b were calculated by the computer software TRACES as the full-widths at half maximum (FWHM) after automatic background removal and $K\alpha_2$ stripping.

It must be pointed out that Eq. (2) is derived under assumption that the instrumental broadening is described

by a Gaussian and the "pure" line profile by a Cauchy function (so-called "Cauchy–Gaussian approximation") [6]. The approximation given by Eq. (2) is recommended for low-resolution geometry diffractometers (essentially early models), but its use with the present data gives better results than other approximations recommended for high-resolution geometry diffractometers (modern machines with "line" X-ray source and Soller slits) [6]. For comparison, we also calculated the instrumental broadening-corrected breadth, $\beta(2\theta)$, by using the "low-angle reflections" reference curve from Fig. 9–9 in Ref. [6]).

For comparative purposes the separation of crystallite size and strain broadening from the "pure" profile breadth $\delta(2\theta)$ [Eq. (2)] or $\beta(2\theta)$ (Fig. 9–9 in [6]) was carried out by four methods. In the first one it was assumed that strain broadening is approximated by a Gaussian function, whereas the nanocrystalline size broadening is better approximated by a Cauchy function [exactly the same as for instrumental broadening, Eq. (2)]. The resulting equation (Ref. [6]) for the crystallite size and strain is

$$\frac{\delta^2(2\theta) \text{ or } \beta^2(2\theta)}{\tan^2\theta_0} = \frac{K\lambda}{L}\left[\frac{\delta(2\theta) \text{ or } \beta(2\theta)}{\tan\theta_0 \sin\theta_0}\right] + 16e^2 \tag{3}$$

where θ_0 is the position of the analyzed peak maximum, λ the X-ray wave length, L the crystallite size and e the "maximum" strain. For all practical purposes the constant K can be set equal to unity [6]. Any available orders of a given reflection may be used to construct a linear plot of $\delta^2(2\theta)$ or $\beta^2(2\theta)/\tan^2\theta_0$ against $[\delta(2(\theta)$ or $\beta(2\theta)]/\tan\theta_0 \sin_0$. From the slope λ/L and ordinate intercept $16e^2$, the crystallite size, L, and strain, e, may be determined. The above method is often customarily referred to as the "Method of Integral Breadths" [1,6,7] and ideally the B and b in Eq. (2), and $\delta(2\theta)$ and $\beta(2\theta)$ should be calculated as the integral breadths rather than the FWHM (as in the present work) but this minor approximation introduces only a negligible difference [6].

The second method was based on the assumption that the crystallite size and strain line profiles are both presumed to be Cauchy and the appropriate equation for the separation of crystallite size and strain takes the following form [6]:

$$[\delta(2\theta) \text{ or } \beta 2\theta)]\cos\theta_0 = \frac{\lambda}{L} + 4e\sin\theta_0 \tag{4}$$

Again, through plotting the crystallite size can be obtained from the intercept and the strain from the slope. Eq. (4) was first proposed by Williamson and Hall [8] and is customarily referred to as the "Williamson-Hall method" [9–12] Although, it was originally derived under assumption that $\delta(2\theta)$ or $\beta(2\theta)$ are calculated from the integral breadths [6,8] most researchers simply use the FWHM instead [9–12].

The third method is quite similar to the second one but now the size and strain line profiles are both presumed to be Gaussian and the appropriate equation takes the following form [6]:

$$[\delta^2(2\theta) \text{ or } \beta^2(2\theta)] \cos^2 \theta_0 = \left(\frac{\lambda}{L}\right)^2 + 16e^2 \sin \theta_0 \qquad (5)$$

As before, one can get both L, and e, from a linear plot.

For the sake of clarity, it must be mentioned that the crystallite size, L, calculated from Eqs. (3)–(5) is the volume-average of the crystallite dimension perpendicular to the diffracting planes (hkl) from which it is calculated ($2\theta_0$), while e is the so-called "upper limit strain" (maximum strain) such that $e = 1.25 <\varepsilon^2>^{1/2}$ where ε is the so-called root-mean-square strain appearing in the much more sophisticated Fourier method of Warren and Averbach applied to the determination of crystallite size and lattice strain [6]

The fourth method is the well-known Scherrer formula [6].

$$L = \frac{0.9\lambda}{\beta(2\theta) \cos \theta_0} \qquad (6)$$

where L is the mean dimension of the crystallites composing the powder, $\beta(2\theta)$ is the breadth (commonly the FWHM or integral breadth) of the "pure" diffraction profile. Only $\beta(2\theta)$ calculated from the b/B ratios (Fig. 9–9 in Ref. [6]), where b/B ratio $\leqslant 0.65$, were taken for calculations. If b/B is large the experimental error in measuring b and B is large [6].

3.3. Crystallite and domain size and microstructural evolution of annealed powders

For the calculation of crystallite size and strain, six fundamental (FCC) reflections, (111), (200), (220), (311), (222), and (400) were used wherever possible. In a few instances of powders annealed at 600°C for 240 min, the measured FWHM of some peaks was equal to or smaller than that of the same peak in the standard powder (annealed 800°C/3 h) XRD scan. These peaks were rejected from the calculations as the strain had been completely relaxed and/or the crystallite size had grown too large. The usage of all available FCC reflections for the size/strain calculations, assumes the so-called "isotropic case" [7], where the powder grains are assumed to be elastically isotropic. This was reported to be the case for the ball milled Nb-metal powders [7].

Fig. 3 shows an example of the comparison of crystallite size/strain calculations for powder milled for 208 h and annealed at 600°C for 60 min according to the Cauchy/Gaussian approximation [Eq. (3)] for $\delta(2\theta)$, also calculated assuming the Cauchy/Gaussian approximation for
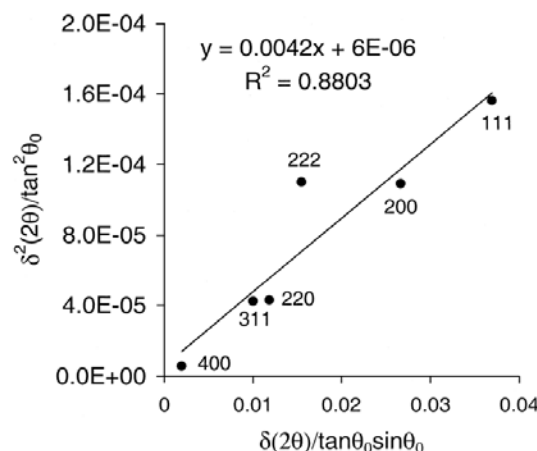

Fig. 3. Crystallite size/strain separation calculation according to the Cauchy/Gaussian approximation given by Eq. (3) using the instrumental broadening-corrected "pure" profile breadth, $\delta(2\theta)$, which was also calculated from the Cauchy/Gaussian approximation [Eq. (2)]. Cubic titanium trialuminide powder milled for 208 h and subsequently annealed at 600°C for 60 min.

the instrumental broadening. The Cauchy/Gaussian approximation for calculating the instrumental broadening-corrected profile breadth, $\delta(2\theta)$, gave slightly better fit than $\beta(2\theta)$ (not shown here) to the crystallite size/strain separation procedure [Eq. (3)] which is also based on the same Cauchy/Gaussian approximation. The crystallite size, L, calculated for $\delta(2\theta)$, and $\beta(2\theta)$ is 37 and 47 nm, respectively. This difference is within a reasonable scatter [6] taking into account all the approximations adopted, so it is difficult to say unambiguously that $\delta(2\theta)$ is better parameter than $\beta(2\theta)$. Nevertheless, since for almost all the annealed powders $\delta(2\theta)$ gave slightly better fit to the linear separation procedure according to Eq. (3) than $\beta(2\theta)$, we will only present results of crystallite size calculation which were obtained using the $\delta(2\theta)$ corrected profile breadth. In addition, fitting procedure in Fig. 3 also shows that the lattice strains [calculated from the intercept according to Eq. (3)] of annealed titanium trialuminide powders are negligible. Even more importantly, a very reasonable fit of the straight line in Fig. 3 to all six reflections taken for calculations, indicates that the annealed powders are quite isotropic, supporting results reported by Pradhan et al. [7] for the nanocrystalline Nb powders.

However, calculations of crystallite size/strain by the so-called "Williamson–Hall method" (Cauchy/Cauchy) [Eq. (4)] and its modification (Gaussian/Gaussian) [Eq. (5)] was unsuccessful for most powders. An example is shown in Fig. 4 for Eq. (4). Very similar plot was obtained for Eq. (5) (not shown here). As seen, on most of the occasions a substantial scatter of data points resulted without any chance of fitting a straight line (isotropic case). Even assuming anisotropic case, i.e. using only the same order of reflection, e.g. (111)–(222)
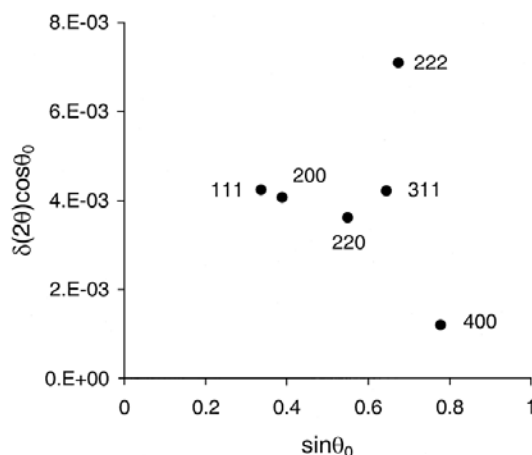
Fig. 4. Crystallite size/strain separation calculation using $\delta(2\theta)$ breadth according to the "Williamson-Hall" method [Cauchy/Cauchy, Eq. (4)]. Powder milled for 208 h and subsequently annealed at 600°C for 60 min.

208–209 h which seem to be the finest ones. The crystallite size after annealing is several-fold larger than the corresponding size after milling [1] which confirms that grain growth of nanocrystals has occurred. In addition, Tables 1 and 2 show that there is no clear correlation between the crystallite sizes calculated from the Cauchy/Gaussian assumption [Eq. (3)] and the Scherrer equation [Eq. (6)]. Since the latter gives quite scattered results, even for small b/B ratios, only the crystallite sizes calculated from Eq. (3) have been considered.

Domain size was calculated for the powder milled for 208 h and isothermally annealed at 600°C for 1, 3, 5, 10, 30, 60, and 240 min. For the domain size calculations two superlattice reflections, (100) and (110) and the Scherrer formula [Eq. (6)] were used. It has been found that the domain size was not influenced by annealing and remained approximately constant (average ~ 20 nm). This average size is on the same order as the average nanocrystallite size of the powder milled for 208 h after isothermal annealing at 600°C (Table 1 and 2; 30–40 nm).

and (200)–(400) pairs for the straight lines [Eq. (4)] in Fig. 4 one obtains extremely diverse values for crystallite size (intercept) and strain (slope). Sometimes, the slopes were such that the resulting intercept was negative. Such a bad fit to the Williamson–Hall is rather surprising since the method has been quite popular for nanocrystals [13]. In view of the observed behavior, the methods given by Eqs. (4) and (5) were discarded and only data on the crystallite size/strain of annealed powders obtained from Eqs. (3) and (6) have been considered.

Tables 1 and 2 show the calculated crystallite size of cubic titanium trialuminide powders milled for various times after annealing at 600°C for 60 and 240 min, respectively. For comparison, the as-milled crystallite sizes are also shown in Table 1. It is quite clear that there is no systematic dependence of the crystallite size after annealing on the prior milling time, except for the annealed crystallite sizes of the powders milled for

Fig. 5 shows the light optical cross-sections of representative powder particles both as-milled and milled + annealed at 600 and 1000°C. As reported in Ref. [1] the majority of particles milled up to ~ 240 h showed two distinct constituents of their microstructure: the "core" and "outer layer" [Fig. 5(a)]. After milling for 386 h most of the particles contained no "core" (so-called "no core" particles) [1]. Annealing at 600°C for 240 min did not bring about any changes recognizable under optical microscope (or even scanning microscope) neither in the "core", "outer layer" nor in the microstructure of the "no core" particles [Fig. 5(b)]. No observable microstructural changes occurred in the majority of particles even after annealing at 1000°C for 60 min [Fig. 5(c)]. Only in a small fraction of the largest powder particles with diameters over $100\,\mu$m did this high-temperature annealing result in the formation of micrometer-sized grains $(4{-}10\,\mu)$, either within the

Table 1
The XRD calculated crystallite size of ball milled and annealed at 600°C for 60 min cubic (L1$_2$) titanium trialuminide powders

Milling time (h)	As-milled crystallite size (nm)	Cauchy/Gaussian [Eq. (3)]			Scherrer [Eq. (6)]		
		Size (nm)	Correlation R^2	Number of XRD reflections used	Size (nm)	Reflections (hkl)	b/B
19	24	38	0.777	6	19/44	(400)/(220)	0.211/0.442
42	19	70	0.855	6	62/65	(220)/(222)	0.529/0.610
105	6	77	0.927	5	107	(400)	0.611
208	3	29	0.925	6	30/47	(200)/(220)	0.439/0.459
208[a]	3	37	0.880	6	23/48	(222)/(220)	0.346/0.462
209	3	47	0.990	6	62/57	(220)/(111)	0.529/0.575
215	3	66	0.459	5	42	(400)	0.377
236	3	96	0.681	6	73/80	(220)/(200)	0.575/0.647
386	3	81	0.944	6	89/118	(220)/(400)	0.619/0.636

[a] Second powder specimen; as-milled crystallite size from Ref. 1.

XRD peak broadening analysis give us **a volume average crystallite size (nanograin size)**. However, more atomic scale insight into the microstructure on nanometric hydrides resulting which were synthesized by various ball milling techniques can be provided by **Transmission Electron Microscopy (TEM) combined with electron diffraction.** A typical TEM analysis for a nanostructured hydride is given by an example below:

CrossMark

High resolution transmission electron microscopy (TEM), energy-dispersive X-ray spectroscopy (EDS) and X-ray diffraction studies of nanocrystalline manganese borohydride (Mn(BH$_4$)$_2$) after mechano-chemical synthesis and thermal dehydrogenation

Amirreza Shirani Bidabadi [a], Andreas Korinek [b], Gianluigi A. Botton [b], Robert A. Varin [a,*]

[a] Department of Mechanical and Mechatronics Engineering, University of Waterloo, Waterloo, Ontario N2L 3G1, Canada
[b] Department of Materials Science and Engineering and Canadian Centre for Electron Microscopy, McMaster University, 1280 Main Street West, Hamilton L8S 4L7, Canada

ARTICLE INFO

ABSTRACT

In order to synthesize manganese borohydride, Mn(BH$_4$)$_2$, mechano-chemical activation synthesis (MCAS) of the (2LiBH$_4$ + MnCl$_2$) powder mixture was carried out by ball milling in a magneto ball mill. Both X-ray diffraction and TEM selected area electron diffraction patterns (SAEDPs) clearly confirm the presence of the Mn(BH$_4$)$_2$ and LiCl phases in the synthesized nanocomposite. No other phases were detected. Bright field high-resolution TEM imaging of the synthesized composite powder particles reveals the presence of nanograins consistent with LiCl and Mn(BH$_4$)$_2$ within the powder particles. Their respective grain sizes, estimated as the equivalent circle diameters (ECD) from the high-resolution TEM micrographs with the corrected sample standard deviations, are within the range of 14.1 ± 3.7 nm and 10.0 ± 2.9 nm for LiCl and Mn(BH$_4$)$_2$, respectively.

The XRD patterns of the thermally dehydrogenated (Mn(BH$_4$)$_2$ + 2LiCl) nanocomposite do not exhibit any Bragg diffraction peaks belonging to either crystalline Mn or B. In contrast, the SAED patterns and EDS elemental maps provide strong evidence that both Mn and B exist in the dehydrogenated powder as crystalline phases α-Mn and β-B, respectively. The results show that the lack of XRD Bragg diffraction peaks is insufficient evidence that the Mn and B elemental products of Mn(BH$_4$)$_2$ thermolysis can be classified as being amorphous.

© 2015 Acta Materialia Inc. Published by Elsevier Ltd. All rights reserved.

1. Introduction

Engineering systems for supplying hydrogen (H$_2$) to fuel cells (FC) in the future Hydrogen Economy [1], based on solid hydrides, are the most attractive long-term solution. Solid state hydride systems exhibit higher H$_2$ volumetric densities than gas or liquid storage and do not have serious safety problems like a very high pressure of 70 MPa for hydrogen gas or large thermal losses for liquid H$_2$ which require a formidable insulation and an open storage system [2–4]. A major problem is that the operating conditions of a Proton Exchange Membrane fuel cell (PEM FC) stack for application in an automotive sector induce serious constraints such as the limited waste heat temperature of barely 70–80 °C and low operating pressure of 1.1–1.8 bar H$_2$ on the automotive H$_2$ storage medium. Furthermore, the US Department of Energy targets for 2017 [5],

for a 300 mile driving distance, require 5.5 wt.% H$_2$ capacity for an entire H$_2$ storage system which translates to at least 10–11 wt.% H$_2$ capacity for the storage material. In addition, "on board" reversibility is required for the automotive H$_2$ storage medium. Unfortunately, a hydride system suitable for an automotive H$_2$ storage, that would simultaneously meet all above requirements, has not been found yet [2–4,6].

Nevertheless, in the past years a few solid state hydride systems have been discovered that could be potentially used as H$_2$ generators in various non-automotive applications, especially those not requiring "on board" reversibility, like for example, those for fuel cell-based stationary auxiliary power systems, off-road vehicles, portable electronics and others.

A complex metal borohydride of potential interest for generating H$_2$ at reasonably low temperatures is manganese borohydride, Mn(BH$_4$)$_2$, that can be synthesized by mechano-chemical activation synthesis (MCAS) during ball milling by solid state reaction between 2 mol LiBH$_4$ and 1 mol MnCl$_2$ [7–12] according to:

* Corresponding author.
E-mail address: ravarin@uwaterloo.ca (R.A. Varin).

$$2LiBH_4 + MnCl_2 \rightarrow Mn(BH_4)_2 + 2LiCl \qquad (1)$$
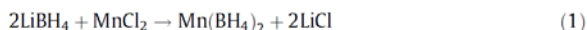
A theoretical H_2 capacity (for 100% purity) of $Mn(BH_4)_2$ is 9.5 wt.% although after synthesis it coexists in a mixture with 2 mol LiCl (Eq. (1)) which reduces the theoretical capacity to 4.76 wt.% H_2 [10]. The ball milled mixture of ($Mn(BH_4)_2$ + 2LiCl) was found to be capable of desorbing up to ~4.5 wt.% H_2 at 100 °C [12] within a very reasonable dehydrogenation time not exceeding 20 h. We also found [12] that the initial ($2LiBH_4$ + $MnCl_2$) mixture in Eq. (1) was very stable during ball milling since it mechanically dehydrogenated only 0.22 wt.% H_2 after 30 min of ball milling which increased only slightly to 0.3 wt.% after 90 min and then stabilized up to 120 min of ball milling. This mechanical dehydrogenation behavior is in contrast to a recently investigated ($2LiBH_4$ + $FeCl_2$) mixture that rapidly desorbed 4 wt.% H_2 within barely 30 min of ball milling [13]. However, for the sake of clarity, it must be mentioned that mass spectroscopy of gas desorbed after thermolysis of $Mn(BH_4)_2$ combined with thermogravimetric analysis shows the presence of small quantities of diborane gas (B_2H_6) mixed with hydrogen gas [10,11] although the signal of hydrogen peak is several hundred times stronger than the diborane gas peak registered with a gas spectrometer [10]. This issue is now under investigation in our laboratory.

Throughout the past few years of studies on the synthesized mixture of ($Mn(BH_4)_2$ + 2LiCl) in our laboratory, only X-ray and synchrotron diffraction were employed for the phase analysis [9,10,12]. Better understanding of the synthesized microstructure on the microscopic/nanometric level would allow us to look for further improvement of the dehydrogenation properties of the studied hydride system. This is an important issue in view of some controversy existing about the microstructure obtained after the synthesis of $Mn(BH_4)_2$ by the mechanochemical reaction of $LiBH_4$ with $MnCl_2$ in [14] where the authors claimed an amorphous structure for the Mn borohydride complex obtained during processing because no X-ray diffraction peaks were observed. Furthermore, amorphous manganese (Mn) and boron (B) species were claimed to be formed after decomposition of $Mn(BH_4)_2$ observed by thermal XRD under flowing helium (He) gas [11] or by in-situ synchrotron radiation [15]. In this work, the presence of either amorphous or crystalline Mn and B could be unambiguously verified by TEM.

The scientific objective of the present study is to obtain a detailed insight into the microstructure of the ($Mn(BH_4)_2$ + 2LiCl) mixture, just after the synthesis by MCAS as well as after subsequent thermal dehydrogenation (thermolysis), using high resolution transmission electron microscopy (HR TEM) combined with energy-dispersive X-ray spectroscopy (EDS) for elemental mapping of the microstructure and X-ray diffraction. It must also be pointed out that, so far, HR TEM investigations have never been reported for those borohydrides synthesized by MCAS during ball milling.

2. Experimental

Lithium borohydride ($LiBH_4$) and manganese chloride ($MnCl_2$) purchased from Alfa Aesar (Canada) with purity of 95% and 99.99%, respectively, were mixed with 2:1 M ratio. Ball milling of the mixture was carried out for 2 h in ultra-high purity hydrogen gas atmosphere (purity 99.999%: $O_2 < 2$ ppm; $H_2O < 3$ ppm; $CO_2 < 1$ ppm; $N_2 < 6$ ppm; CO < 1 ppm; THC < 1 ppm) at ~300 kPa pressure in the magneto-mill, Uni-Ball-Mill 5, manufactured by A.O.C. Scientific Engineering Pty Ltd., Australia [2,16–18]. The strong impact mode (IMP68) with two magnets positioned at 6 and 8 o'clock, at the distance from the vial of ~10 and ~2 mm, respectively was used in the milling process. The powder mixture was loaded into an air-tight milling vial with an O-ring and equipped with a pressure valve mounted on the lid. Four hardened

steel balls were placed in the vial with the ball-to-powder weight ratio (R) of 132 and the rotational speed of milling vial of ~200 rpm. The vial was continuously cooled by an air fan during milling process. In order to avoid reactions between the powder samples and moisture or oxygen from air, all processes during preparation of the samples were handled in a glove box containing moisture-absorbing Drierite granulated compound. Before handling, the glove box was purged a few times with high purity argon gas (99.999% purity) in order to minimize any possible contamination by moisture or oxygen from air.

The hydrogen thermal desorption was evaluated by means of a second generation volumetric Sieverts-type apparatus custom-built by A.O.C. Scientific Engineering Pty Ltd., Australia [2,3,6,9,10,12,13]. This apparatus, built entirely of 316 austenitic stainless steel, allows loading a powder sample into a stainless steel reactor in a glove box under high purity argon and its subsequent transfer to the main unit in a sealed reactor without any exposure to the environment. Approximately 30–40 mg sample was used in a desorption test. Before starting the desorption test, the inner tubing of the apparatus was evacuated and purged 4 times with hydrogen. The furnace of the apparatus was heated separately to the desired test temperature and subsequently inserted onto a tightly sealed powder sample reactor inside which an atmospheric pressure of 1 bar H_2 was kept. The powder sample in the reactor usually reaches the furnace temperature within ~400 s in the temperature range of 100–200 °C which is negligible compared to desorption completion time. Hence, the test can be considered as isothermal. Desorption curves were corrected for the hydrogen gas expansion because of increase in temperature. The amount of desorbed hydrogen was calculated from the ideal gas law as described in detail in [2,3,6,9,10,12,13] and expressed in wt.% with respect to the *total* weight of powder sample. The calibrated accuracy of desorbed hydrogen capacity is about ±0.1 wt.% H_2 and that of temperature reading and stabilization ±0.1 °C.

The crystalline properties of the powders were characterized by a Bruker D8 X-ray diffractometer using a monochromated CuKα_1 radiation ($\lambda = 0.15406$ nm) with an accelerating voltage of 40 kV and a current of 30 mA. The scan range was from $2\theta = 10$ to 90° and the rate was 1.2 min^{-1} with a step size of 0.02°. The powder sample was loaded in the glove box into a home-made brass holder with Cu/glass plates and Kapton window transmittable to X-rays in the upper part of the sample holder.

Morphology and compositional analysis of synthesized mixture after ball milling were conducted by scanning electron microscope (Zeiss ULTRA plus) and energy dispersive X-ray spectroscopy (EDS), respectively. The samples were dispersed on a sticky carbon tape under argon atmosphere in a glove box and pictures taken under secondary electron mode (SE) with an accelerating voltage of 10 kV.

Samples for high resolution transmission electron microscopy (HR TEM) were prepared by two different methods. The first one was a wet method where a proper solvent was required that allows for dispersing the agglomerates into individual powder particles by ultrasonication. The diethyl ether (Et_2O) solvent was adopted in this work which was already used for solvent (wet) chemical separation of complex alanate hydrides from salts [19]. The ball milled powder was dispersed in Et_2O and distributed on an amorphous carbon grid.

The second one was a dry method in which the dry powders were directly dispersed onto the amorphous carbon grids.

In both methods, preparations were done outside such that the samples were in air for a few minutes during the transfer to the microscope. Electron microscopy studies were performed with a HR TEM FEI Titan microscope at 300 kV ($\lambda = 0.0197$ Å), equipped with a CEOS image corrector and an Oxford INCA X-sight EDS system and the energy filter Gatan Tridiem GIF. Samples were imaged

using a Gatan LN_2 holder which decreased the beam induced sample damage of the hydride powder. A fast Fourier transform (FFT) was used for obtaining digital selected-area electron diffraction patterns (SAEDPs) from the high resolution TEM micrographs by applying the ImageJ software [20]. The grain (crystallite) size of the $Mn(BH_4)_2$ and LiCl phases from the HR TEM images was estimated as the equivalent circle diameter, $ECD = (4A/\pi)^{1/2}$, where A represents the projected particle area which was measured using the ImageJ software [20]. The corrected sample standard deviation for an average ECD value was also calculated.

3. Results and discussion

3.1. Microstructure of powders after ball milling (BM)

The energy of milling in the magneto ball mill, Uni-Ball Mill 5, employed in the present study can be controlled by changing the angular positions of magnets and the number of balls in each vial [2]. Based on the semi empirical model reported in [21] the amount of energy per hour for the IMP68-4B-R132 milling mode used in this work, that can be injected into the powder, is $Q_{TR} = 72.8$ kJ/g h. Since the duration of ball milling in this work was 2 h, the total milling energy input into the powder was 145.6 kJ/g for each powder sample.

We already reported [12] that the average powder particle size for $LiBH_4$ and $MnCl_2$ was 238.5 ± 109.7 µm and 19.1 ± 9.8 µm, respectively. After ball milling (BM) with the energy input $Q_{TR} = 145.6$ kJ/g the average powder particle size of the BM mixture decreased to 7.5 ± 2.6 µm [12]. Fig. 1Sa (Supplement) shows the SEM secondary electron image of powder after ball milling in the present work with the energy input $Q_{TR} = 145.6$ kJ/g. Fig. 1Sb and c (Supplement) show the results of the EDS chemical analysis from two selected areas of the BM mixture, where the EDS spectrum of boron (B), chlorine (Cl) and manganese (Mn) are clearly observed. The spectra of carbon (C) and oxygen (O) are most likely arising from a carbon tape used as a substrate for powders analysis. Since the EDS detector cannot detect presence of elements with atomic number less than 5, the spectrum of Li in this experiment is not detected. The EDS spectra for the ball milled powder sample show the presence of Mn and Cl which, most likely, reside in the synthesized $Mn(BH_4)_2$ and LiCl phases, respectively, that were formed during ball milling as a result of MCAS according to reaction (1).

Fig. 1 shows the XRD patterns of the as-received ($2LiBH_4 + MnCl_2$) powder mixture and the same mixture after ball milling. It confirms formation of both $Mn(BH_4)_2$ and LiCl after MCAS by ball milling. The as-received pattern shows the diffraction peaks of orthorhombic $LiBH_4$ (space group Pnma, $a = 7.17858(4)$, $b = 4.4368e\ 2(2)$, $c = 6.80321(4)$ Å) [22] and rhombohedral $MnCl_2$ (space group R-3 m, $a = 3.7061$, $b = 3.7061$, $c = 17.569$ Å) [23]. It can be seen that after 2 h ball milling with the energy input $Q_{TR} = 145.6$ kJ/g, the diffraction peaks of the constituent powders disappeared while the $Mn(BH_4)_2$ and LiCl peaks evolved. The XRD pattern evolution confirms the synthesis of $Mn(BH_4)_2$ and LiCl as described by reaction (1). The identification of $Mn(BH_4)_2$ was based on the crystallographic data reported in [7,14,24] which show that $Mn(BH_4)_2$ has a trigonal/hexagonal lattice structure (the space group $P3_112$) with the lattice parameters $a = 10.435(1)$ Å and $c = 10.835(2)$ Å.

As mentioned earlier, the diethyl ether (E_2O) solvent was used in a wet method in order to breakdown the powder sample into smaller pieces, most ideally, into individual particles having thickness transparent to the electron beam. The transmission electron microscopy (TEM) micrographs of the synthesized powder prepared by a wet method using Et_2O are shown in Fig. 2S (Supplement). It appears that the Et_2O solvent reacted with the ball milled powder damaging the surface of powder particles. Apparently, the wet method using Et_2O seems not to be suitable for extracting individual powder particles form the synthesized powder for TEM study. It was discarded from further consideration.

Fig. 2a presents the TEM micrograph of two partially overlapped powder particles, a smaller one with ECD = 0.63 µm and a larger particle with ECD = 1.14 µm, which were extracted from the synthesized nanocomposite ($Mn(BH_4)_2 + 2LiCl$) powder without using any solvent (dry method). The sample looks much better although it shows some degree of beam damage and the presence of amorphous material. Apparently, the dry method is much more effective for extracting undamaged particles from the synthesized powder than the wet method. Fig. 2b shows the selected area electron diffraction pattern (SAEDP) from the larger particle area indicated by a red arrow in Fig. 2a. A number of interplanar spacings ($d_{(hkl)}$), which are shown in the left upper corner of Fig. 2b, corresponding to various diffracting (hkl) planes in the crystalline lattice of the LiCl phase, were experimentally calculated from the SAEDP and they are depicted by calculated powder ring patterns in the SAEDP in Fig. 2b analogous to those obtained from X-ray powder
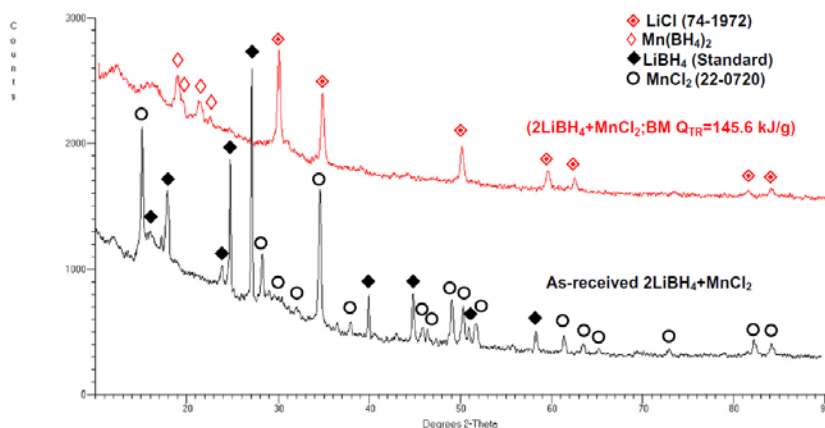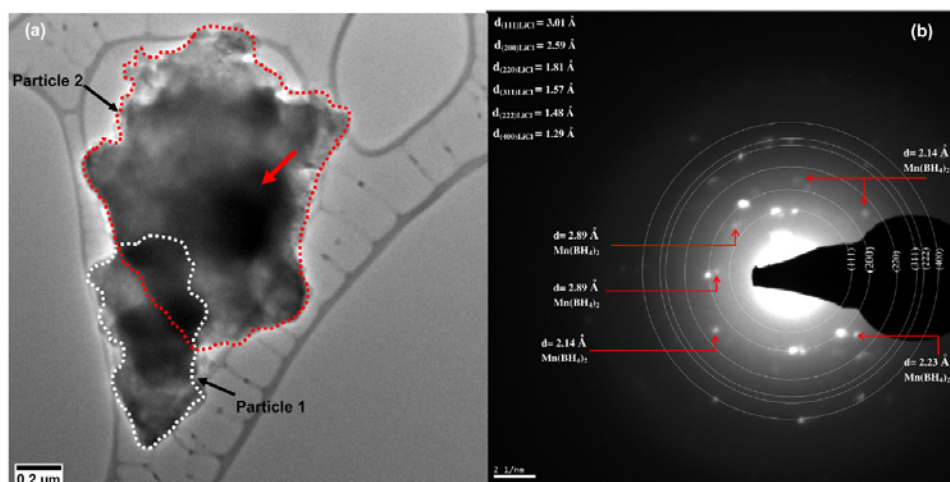

Fig. 1. XRD patterns of the as received ($2LiBH_4 + MnCl_2$) mixture and the same mixture after ball milling with an energy input $Q_{TR} = 145.6$ kJ/g (2 h).

Fig. 2. (a) TEM micrograph of two partially overlapping powder particles which were extracted without using solvent (dry method) from the synthesized nanocomposite (Mn(BH$_4$)$_2$ + 2LiCl). (b) Corresponding selected area diffraction (SAED) pattern.

diffraction. Each calculated ring corresponds to a interplanar spacing, $d_{(hkl)}$. They are clearly consistent with the crystal lattice spacings from ICDD (JCPDC) card #74-1972 for LiCl which is used as a standard in our XRD analysis.

Fig. 3a shows high-resolution TEM image of individual nanograins/crystallites residing in one of the particles in Fig. 2a. The area on the image exhibiting the same orientation of the lattice planes, visible under high resolution, was corresponding to one individual nanograin and the contours of nanograins are delineated by a broken line. Subsequently, the digital diffraction using a fast Fourier transform (FFT) from the entire image, that includes all nanograins visible within the frame, was performed and is shown in the top inset. The calculated diffraction rings using the ImageJ software, visible on the digital diffraction in Fig. 3b, were identified as corresponding to LiCl by calculating the ratio of the diameter of the second ring further from the center, corresponding to the LiCl (2 0 0) lattice plane and inverse of its lattice spacing, $1/d_{(200)}$, to the diameter of the first ring near the center, corresponding to the LiCl (1 1 1) lattice plane ($1/d_{(111)}$), which is equal to 1.15. This particular ratio exactly fits with the ratio of $d_{(111)}/d_{(200)}$ of the fcc structure of LiCl phase in our material. Since Mn(BH$_4$)$_2$ has diffraction spots at lower 2θ angles or correspondingly larger $d_{(hkl)}$ spacings (Table 1) than LiCl, it must have diffraction spots closer to the center of FFT diffraction pattern in the inset as compared to LiCl. As a results, the four digital white diffraction spots identified by the arrows in the inset in Fig. 3b are corresponding to Mn(BH$_4$)$_2$. Subsequently, each individual nanograin was identified as belonging either to LiCl or Mn(BH$_4$)$_2$ based on respective digital diffraction using FFT performed on each individual nanograin and subsequent calculation of the ring diameter/interplanar spacing ratios. The grains contoured by a dotted red line correspond to LiCl and their digital diffraction spots all have the ratio near 1.15, characteristic of an fcc-type lattice (LiCl). The nanograins delineated by a white dotted line belong to Mn(BH$_4$)$_2$ and their FFT diffraction spots always appear at one of the positions of the four FFT diffraction spots near the center (see white arrows) and they do not exhibit the fcc ratios.

For additional confirmation of the correctness of the FFT analysis in Fig. 3a, an TEM SAEDP was taken exactly from the area of nanograins visible in Fig. 3a and is shown in Fig. 3c. A number of interplanar spacings ($d_{(hkl)}$), which are shown in the left upper corner of Fig. 3c, corresponding to various diffracting (hkl) planes in

the crystalline lattice of the LiCl phase, were experimentally calculated from the SAEDP and they are overlaid with the calculated powder ring patterns in Fig. 3c.

For the unambiguous identification of Mn(BH$_4$)$_2$ from the electron diffraction SAEDPs in Figs. 2b and 3c, we used the 2θ values extracted from the synchrotron radiation diffraction pattern reported in [10] for the synthesized (Mn(BH$_4$)$_2$ + 2LiCl) nanocomposite which are tabulated in the first column in Table 1. Using the synchrotron 2θ values and the synchrotron radiation wavelength from [10] the plane spacings $d_{(hkl)}$ for Mn(BH$_4$)$_2$ were calculated from the Bragg's law and are also listed in the second column in Table 1. The third column in Table 1 contains the $d_{(hkl)}$ values experimentally obtained from the SAEDPs in Figs. 2b and 3c. Unfortunately, a large background in the scattered intensity at low angles in the SAEDP in Figs. 2b and 3c does not allow to recognize the first few diffraction spots corresponding to the highest intensity peaks for Mn(BH$_4$)$_2$ at 2θ = 18.9, 19.5 and 21.2° which correspond to the $d_{(hkl)}$ interplanar spacing larger than 3.46 Å (Table 1). However, the other diffraction spots for Mn(BH$_4$)$_2$ at larger 2θ angles ($d_{(hkl)}$ smaller than 3.46 Å) are well visible in Figs. 2b and 3c and are summarized in the third column in Table 1. The experimental $d_{(hkl)}$ interplanar spacings for Mn(BH$_4$)$_2$, obtained from the electron SADPs in Figs. 2b and 3c, are in good agreement with the corresponding interplanar spacings calculated from the synchrotron radiation diffraction (the reader can compare the second and third column in Table 1). This excellent agreement confirms unambiguously the presence of crystalline Mn(BH$_4$)$_2$ after mechano-chemical synthesis, in the microstructure of the ball milled samples.

We calculated the average nanograin/crystallite size (expressed as ECD) of each constituent phase LiCl and Mn(BH$_4$)$_2$ from several HR TEM micrographs which exhibited a number of LiCl and Mn(BH$_4$)$_2$ grains similar to those visible in Fig. 3a. From the digital SAED patterns using FFT on a few HR TEM micrographs (similar to an example in Fig. 3c), we were able to identify fourteen grains of LiCl and eleven grains of Mn(BH$_4$)$_2$. For LiCl and Mn(BH$_4$)$_2$ the average ECD equals 14.1 ± 3.7 and 10.0 ± 2.9 nm, respectively. By comparison, the crystallite size for LiCl and (MnBH$_4$)$_2$, synthesized in the powder ball milled with Q_{TR} = 145.6 kJ/g, exactly like in the present work, was estimated by using the Scherrer formula from the XRD patterns to be equal to 30.6 ± 5.6 and 18 ± 1 nm, respectively,
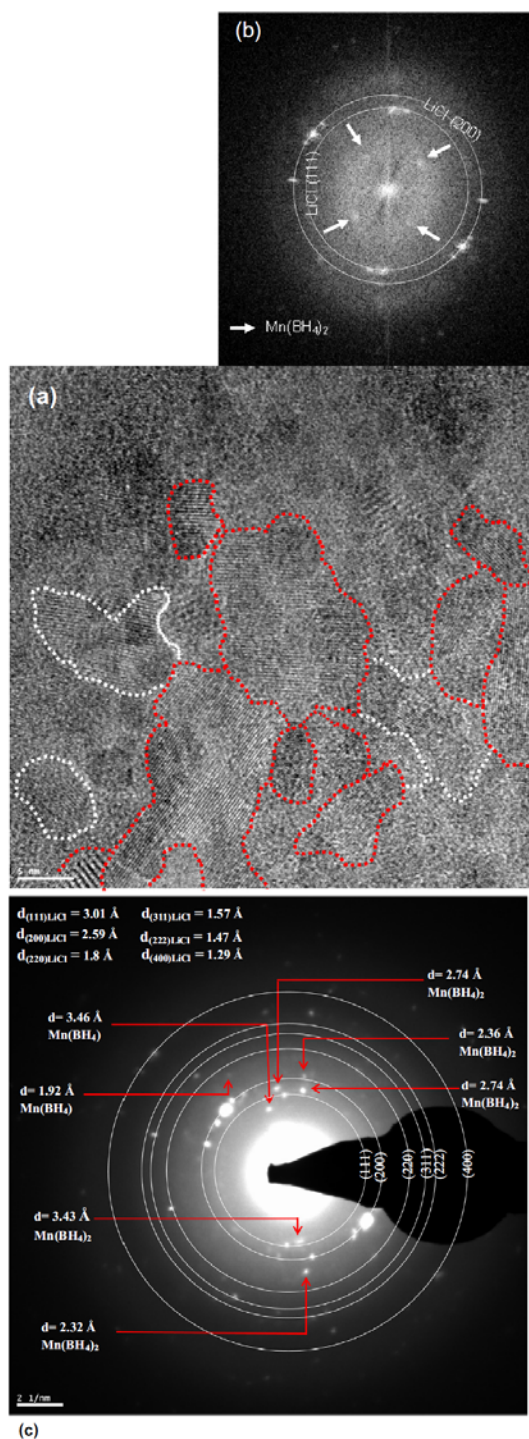
$d_{(111)LiCl} = 3.01$ Å $d_{(311)LiCl} = 1.57$ Å
$d_{(200)LiCl} = 2.59$ Å $d_{(222)LiCl} = 1.47$ Å
$d_{(220)LiCl} = 1.8$ Å $d_{(400)LiCl} = 1.29$ Å

Fig. 3. (a) High resolution TEM image of a particle extracted from the synthesized nanocomposite (Mn(BH$_4$)$_2$ + 2LiCl) powder (marker is 5 nm). (b) A digital SAEDP using a fast Fourier transform (FFT) of the whole image in (a). (c) SAEDP from the particle imaged in (a).

as reported in our previous article [12]. The average ECD values for both the LiCl and (MnBH$_4$)$_2$ phases, estimated using HR TEM technique in this work, are apparently smaller than the average crystallite size values estimated from the XRD Scherrer formula. This could be envisaged because two dissimilar methods were used for estimating a nanograin size which is well discussed in [25–27]. The important finding is that the HR TEM grain size analysis performed in this work confirms that both the LiCl and Mn(BH$_4$)$_2$ phases are nanocrystalline after being formed during mechano-chemical synthesis of the initial (2LiBH$_4$ + MnCl$_2$) mixture.

3.2. Isothermal dehydrogenation and microstructure of powders after annealing

Fig. 3S (Supplement) shows the isothermal volumetric desorption curves under 1 bar H$_2$ pressure at 100 °C (black), 150 °C (blue) and 200 °C (red) for the synthesized nanocomposite (Mn(BH$_4$)$_2$ + 2LiCl). The observed total quantity of desorbed hydrogen is 4.69 wt.% (after 18.7 h), 4.40 wt.% (after 9.2 h) and 4.57 wt.% (after 12.4 h) at 100, 150 and 200 °C, respectively. The time required for desorbing 4.00 wt.% H$_2$ is 2.3 h at 100 °C but decreases to 0.4 h for both 150 °C and 200 °C. After the same time duration of 2 h, the quantity of 3.9, 4.1 and 4.1 wt.% H$_2$ at 100, 150 and 200 °C was desorbed, respectively. It is to be pointed out that as mentioned earlier, because of mechanical dehydrogenation on the order of 0.3 wt.% H$_2$ after 2 h of milling [12] all thermally desorbed H$_2$ quantities should be in reality corrected upwards by about 0.3 wt.% for the total H$_2$ capacity.

It has been proposed [5,6,7–12,14] that the nanocomposite (Mn(BH$_4$)$_2$ + 2LiCl) synthesized in reaction (1) decomposes with a release of H$_2$ according to reaction (2):

$$Mn(BH_4)_2 + 2LiCl \rightarrow Mn + B + 4H_2 + [2LiCl] \qquad (2)$$
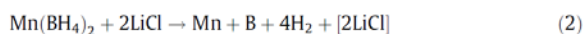
where the square bracket means that LiCl remains unchanged in the nanocomposite. The maximum theoretical capacity of reaction (2) is 4.76 wt.% H$_2$ [12].

However, as mentioned earlier in Introduction, the release of diborane gas (B$_2$H$_6$) in a mixture with H$_2$ was reported [10,11,15] which was observed using combined gas mass spectroscopy (MS) and thermogravimetric analysis (TGA) that modifies the reaction path with B$_2$H$_6$ to reaction (3):

Table 1
Experimental 2θ values (from [10]) and the calculated lattice spacings, $d_{(hkl)}$, for Mn(BH$_4$)$_2$ from synchrotron radiation and experimental $d_{(hkl)}$ from SAEDP in this work.

Experimental 2θ values from synchrotron radiation ($\lambda = 0.73065$ Å) pattern in [10] for $n = 2$	Calculated $d_{(hkl)}$ (Å) for Mn(BH$_4$)$_2$ from the Bragg's law using $\lambda = 0.73065$ Å for synchrotron	Experimental $d_{(hkl)}$ (Å) for Mn(BH$_4$)$_2$ from SAEDP in this work
4.714	8.88311	–
7.992	5.24238	–
8.937	4.68901	–
9.207	4.55178	–
10.017	4.18454	–
10.584	3.96095	–
12.12	3.46051	3.46
12.201	3.43790	3.43
14.360	2.92291	2.89
15.340	2.73719	2.74
17.771	2.36530	2.36
18.090	2.32380	2.32
18.850	2.23091	2.23
19.681	2.13769	2.14
20.360	2.06701	–
21.631	1.94696	–
21.840	1.92847	–